SAND2013-10488C

Experimental methods to quantify particle positional and displacement uncertainty along the depth direction in digital in-line holography

Daniel R. Guildenbecher[1], Phillip L. Reu[2], Martin B. Nemer[3]
Sandia National Laboratories, Albuquerque, New Mexico, 87185

Jian Gao[4], and Jun Chen[5]
Purdue University, West Lafayette, Indiana, 47907

Digital in-line holography (DIH) is an optical technique for the measurement of three-dimensional (3D) particle fields. Although DIH has many potential applications, widespread use of the technique is hindered by relatively high uncertainty in the measured particle depth. Here we present new experimental methods to quantify the depth uncertainty by comparing measured particle trajectories to predicted trajectories for a simple, rotational flow. When using the hybrid method of particle detection, the measured depth uncertainty is similar to previous results from stationary particles with uniform displacement. Here, the addition of relative particle motion provides further insight into experimental sources of depth uncertainty.

Nomenclature

d	=	particle diameter
$\bar{d}$	=	mass median diameter
E	=	complex amplitude of the numerically reconstructed wave
E_o, E_r	=	complex amplitude of the object wave and reference wave
x, y	=	transverse spatial coordinates
z	=	depth coordinate along the optical axis
z_c	=	depth coordinate along the optical axis corrected for refractive interface effects
λ	=	recording wavelength
ω, r	=	angular velocity and radius of the particle trajectory
ω_0, r_0	=	angular velocity and radius of the stir rod
ξ,η	=	transverse spatial coordinates in the hologram plane

I. Introduction

Digital in-line holography (DIH) is an optical technique in which a collimated laser illuminates an object field. The resulting diffraction pattern is digitally recorded, and numerically refocused via solution of the diffraction equations.[1,2] For example, Figure 1(a) shows experimental holograms of the impact of a water drop on a thin film.[3] In Figure 1(b), these holograms are numerically refocused to a distance of z = ### mm along the optical axis. In-focus features of the secondary drops and the crown-morphology are revealed. Finally, by searching through a range of z-positions, algorithms can be defined to automatically extract the in-focus features at each z, resulting in the three-dimensional (3D) reconstruction of the particle field shown in Figure 1(c). Here, velocities are obtained by matching detected particle locations from two holograms recorded with short inter-frame time. Full details on these results can be found in Guildenbecher *et al*.[3]

[1] Senior Member of Technical Staff, Mail Stop 0840.
[2] Principle Member of Technical Staff, Mail Stop 1139.
[3] Principle Member of Technical Staff, Mail Stop 0346..
[4] Graduate Research Assistant, School of Mechanical Engineering, 500 Allison Road.
[5] Assistant Professor, School of Mechanical Engineering, 500 Allison Road.

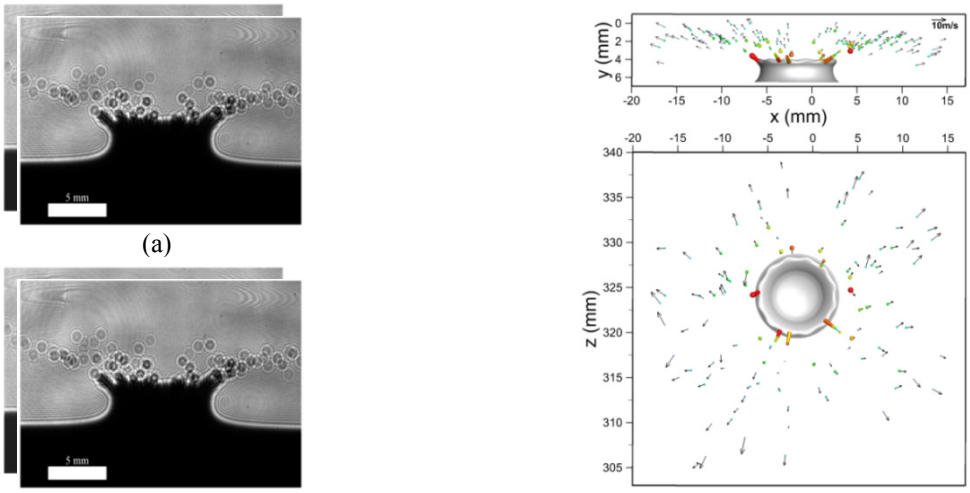

(a)

(b)

(c)

Figure 1. (a) Digital in-line holograms of the impact of a drop on a thin film, (b) the corresponding amplitude images when the holograms are numerically refocused to z = ### mm, and (c) the reconstructed 3D particle positions and velocities.[3]

A major challenge in DIH is the depth of focus problem as discussed by Katz and Sheng.[2] Due to the limited effective angular aperture from which individual particle images are reconstructed,[4] the intensity within the reconstructed particle images varies slowly with respect to depth, z. Consequently, methods which search through the expected particle depths and apply focus metrics to extract in-focus particle images[5-8] tend to suffer from high uncertainty in the measured particle z-locations. This is illustrated in Figure 1(c) where the measured z-velocity component shows significantly higher uncertainty compared to the in-plane velocity components (x-y velocities).

For interpretation of DIH measurements, it is crucial that this z-uncertainty is well quantified. In our previous works, z-uncertainty has be quantified using simulated holograms and experiments applied to known particle fields.[7,8] In the former, all aspects of the simulated particle(s) are known *a-priori* including the particle size, morphology, and x, y, z location. Consequently, reconstructions of simulated holograms can be used to estimate the uncertainty of all of these quantities. However, it is difficult, if not impossible, to construct simulations which incorporate all sources of experimental uncertainty, such as the effects of aberrations, particle overlap, particle motion, and noise introduced by dust on the optics, bad pixels, etc. For this reason, experimental quantification of uncertainty is also necessary. In our previous work, uncertainty has been experimentally quantified using nearly-stationary particles immersed in viscous silicone oil. By recording multiple holograms after displacing the particle field by a known amount in the z-direction using a linear traverse, matching between reconstructed particle locations was used to quantify the uncertainty in the measured z-displacement (Δz). However, because the overall z-location of each particle was not known *a-priori*, these methods could not be used to experimentally validate the accuracy of the measured z-position.

Here, new experimental methods are proposed which can be utilized to validate not only the measured z-displacement but also estimate the accuracy of the overall measured z-position. The work begins with a discussion of the experimental configuration. Next the digital holographic processing methods are briefly reviewed. Finally, the results are applied to derive experimental estimates of z-uncertainty.

II. Experimental Configuration

The chosen experimental configuration for investigation of z-uncertainty in DIH is shown in Figure 2. Similar to our previous work,[3,9] the output from a flash-lamp pumped, frequency-doubled Nd:YAG laser (Litron Nano S 65-15 PIV, ~5ns pulse duration) is spatially filtered and collimated to a beam diameter of 50.8 mm. This collimated beam passes through a particle field consisting of polystyrene particles (particle density, $\rho_p = 1050$ kg/m^3) immersed in clear, viscous silicone oil (fluid density, $\rho_f = 971$ kg/m^3 and viscosity, $\mu_f = 9.71$ Pa·s), contained in a glass cuvette with inner dimensions of 50×50×50 mm (Hellma Analytics model 704.003-OG). Here, two particle fields are considered with mass median diameters of $\overline{d} = 465$ μm and $\overline{d} = 118$ μm, as measured with a Malvern Mastersizer 2000. In both cases, a sparse particle field is considered with a concentration of approximately 3.3 particles/cm^3 and 2.9 particles/cm^3 for the $\overline{d} = 465$ μm and $\overline{d} = 118$ μm cases, respectively.

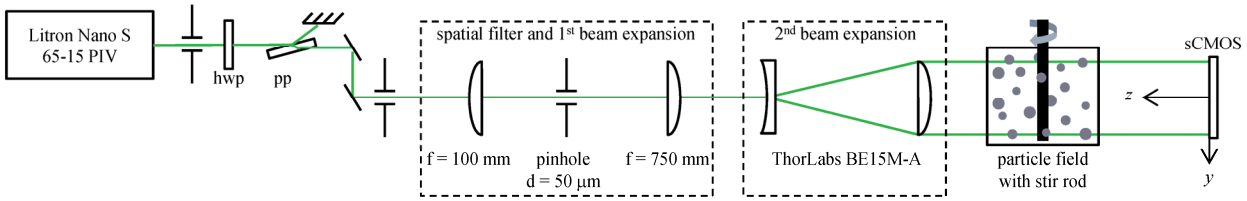

Figure 2. Experimental configuration for the measurement of a swirling particle field using DIH.

The particles are brought into motion by the rotating spindle of a Brookfield Viscometer placed into the center of the cuvette as illustrated in Figure 2. The chosen spindle (RV-7) consists of a stainless-steel rod with uniform radius $r_0 = 1.58$ mm, as measured with precision calibers. The rod is rotated at a constant angular velocity of $\omega_0 = 100$ rpm. This configuration results in a flow pattern which appears similar to the classic Taylor-Couette flow, with the exception that the outer walls are square, rather than cylindrical. As a consequence, secondary corner vortices are expected. To ensure the lateral extent of the secondary vortices did not cross into the experimental measurement volume, a computational fluid dynamics (CFD) simulation was completed using Sandia National Laboratories' ARIA finite-element based multiphysics solver.[10] The Stokes equations were solved on an unstructured, 3D grid consisting of approximately 1.2 million tetrahedral Q1Q1 elements with pressure stabilization. Figure 3 shows the computational results, along with the effective measurement volume of the holography system. From this result we conclude that within the experimental measurement volume, streamlines are nearly circular, which justifies the later use of circular trajectories to model the flow. The CFD computed horizontal extent of the secondary vortices is found to be ~5% of the width of the cuvette, which is consistent with the literature.[11,12]

Gravitational settling and centripetal forces are expected to cause the motion of the embedded particles to deviate slightly from the fluid motion. For spherical particles, the Stokes flow terminal velocity in the y-direction can be estimated as $v_{term} = g(\rho_p - \rho_f)d^2/18\mu_f$, where g is the gravitational acceleration and d is the particle diameter. For the conditions considered here, $v_{term} = 0.06$ µm/s and 1.0 µm/s, for the $\bar{d} = 118$ µm and $\bar{d} = 465$ µm particles, respectively. Data acquisition requires 15.33 s; therefore, over the experimental duration, particles are expected to deviate from the fluid motion by at most 15 µm in the y-direction. Further, along the circular path of the particle, viscous drag supplies the centripetal force such that the particle radial slip velocity is given by $v_{slip} = \rho_p d^2 r\omega^2/18\mu_f$, where r and ω is the radius and angular velocity of the particle, respectively. The maximum v_{slip} occurs at $r = r_0$, $\omega = \omega_0$ and is equal to 0.01 µm/s and 0.2 µm/s, for the $\bar{d} = 118$ µm and $\bar{d} = 465$ µm particles, respectively. Therefore, over the experimental duration particles are expected to deviate from the fluid motion by most 3 µm in the radial-direction. As shown in the following sections, these deviations are significantly less than the observed measurement uncertainties, and therefore particles can be assumed to follow the flow within the precision of the measurement.

220 hologram images are captured at 15 Hz with a LaVision Imager sCMOS (2560×2160 pixels, 6.5 µm pixel pitch) placed at a z-distance of approximately 220 mm from the center of the cuvette. Figure 4 shows select hologram images for the case when $\bar{d} = 465$ µm. The motions of individual particles are easily tracked, as illustrated by the particle selected in the white box in Figure 4. Note, images in Figure 4 are displayed at $1/10^{th}$ the actual recording rate.

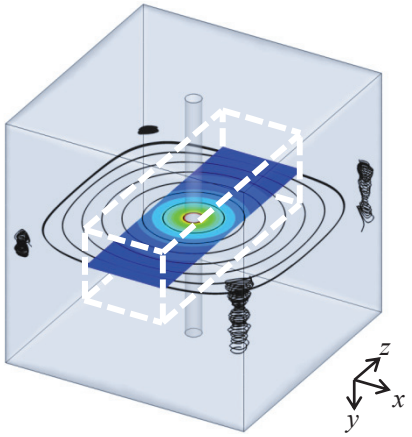

Figure 3. Predicted flow field, where white dotted lines show the effective measurement volume of DIH (16.64 mm in the *x*-direction, 14.04 mm in the *y*-direction, 50 mm in the *z*-direction) and black lines show predicted streamlines which originate within the center *x*-*z* plane colored by total velocity.

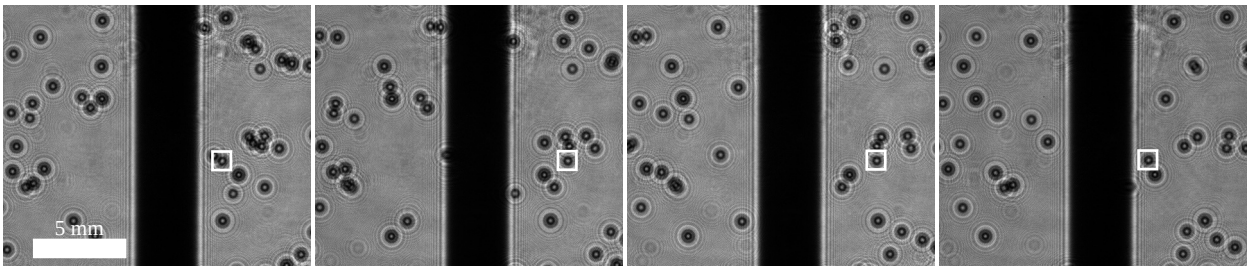

(a) (b) (c) (d)

Figure 4. Select experimental holograms for the case where $\bar{d}$ = 465 μm. Time between images is 0.67 s. White boxes highlight the motion of a single particle.

III. Processing Methods

A hologram, h, is formed from the interference between a collimated laser beam and the portion of the beam scattered by particles in its path,

$$h(\xi,\eta) = \left|E_r + E_o(\xi,\eta)\right|^2 = \left|E_r\right|^2 + \left|E_o(\xi,\eta)\right|^2 + E_o(\xi,\eta)E_r^* + E_r E_o^*(\xi,\eta). \tag{1}$$

Here, the complex amplitude of the scattered light is referred to as the object wave, E_o, while the portion of the beam which propagates through the particle field undisturbed is referred to as the reference wave, E_r. Finally, (ξ,η) are the spatial coordinates in the hologram plane.

In the numerical reconstruction, the hologram is multiplied by the complex conjugate of the reference wave, E_r^*, resulting in an expression of complex amplitude,

$$h(\xi,\eta)\cdot E_r^* = \left[\left|E_r\right|^2 + \left|E_o(\xi,\eta)\right|^2\right]E_r^* + E_r^{*2}E_o(\xi,\eta) + \left|E_r\right|^2 E_o^*(\xi,\eta). \tag{2}$$

This complex amplitude is numerically propagated to any distance, z, through solution of the diffraction equation,

$$E(x,y,z) = \frac{1}{j\lambda}\int_{-\infty}^{+\infty}\int_{-\infty}^{+\infty} h(\xi,\eta)\cdot E_r^* \frac{\exp\left\{jk\sqrt{(\xi-x)^2+(\eta-y)^2+z^2}\right\}}{\sqrt{(\xi-x)^2+(\eta-y)^2+z^2}}\,d\xi d\eta. \tag{3}$$

Here, $E(x,y,z)$ is the reconstructed complex amplitude at z; λ is the wavelength; and k is the wavenumber, $k = 2\pi/\lambda$. In Eq. (3) the diffraction equation is written using the Rayleigh-Sommerfeld diffraction kernel. In many situations the paraxial assumption can be applied to yield the somewhat simpler Kirchhoff-Fresnel form,

$$E(x,y,z) = \frac{\exp\{jkz\}}{j\lambda z}\int_{-\infty}^{+\infty}\int_{-\infty}^{+\infty} h(\xi,\eta)\cdot E_r^* \exp\left\{\frac{jk}{2z}\left[(\xi-x)^2+(\eta-y)^2\right]\right\}d\xi d\eta. \tag{4}$$

Equations (3) and (4) can be numerically solved as

$$E(x,y,z) = \Im^{-1}\left\{\Im\left\{h(x,y)\cdot E_r^*\right\}\cdot G(z)\right\}, \tag{5}$$

where $\Im$ and $\Im^{-1}$ denote the Fourier transform and inverse Fourier transform, respectively. These are typically numerically evaluated with the fast Fourier transform (FFT). $G(z)$ is the analytic expression of the diffraction kernel. For example, for the Rayleigh-Sommerfeld kernel,

$$G(z) = \exp\left\{jkz\sqrt{1-(\lambda m/M\Delta\xi)^2-(\lambda n/N\Delta\xi)^2}\right\}, \tag{6}$$

where (m,n) are the pixel coordinates. Finally, reconstructed images are visualized using the amplitude, $A = |E|$ or intensity, $I = |E|^2$.

For example, Figure 5(a) show the reconstructed amplitude image when the hologram in Figure 4(b) is numerically refocused to z = 211.96 mm using Eq. (5). Interestingly, in this image, the particle appears aberrated with a noticeable astigmatism. The source of this aberration is still being investigated. Nevertheless, here the method proposed De Nicola *et al.*[13] is used to compensate for the aberrations by introducing *ad-hoc* corrections to the spatial frequency terms in Eq. (6),

$$G(z) = \exp\left\{jk\sqrt{z^2-(z+z_x)^2(\lambda m/M\Delta\xi)^2-(z+z_y)^2(\lambda n/N\Delta\xi)^2}\right\}. \tag{7}$$

Here, z_x and z_y are focus corrections in the x- and y-directions, respectively. Trial and error is used to find the optimal as z_x = -1 mm and z_y = 1 mm, resulting in the corrected particle image shown in Figure 5(b).

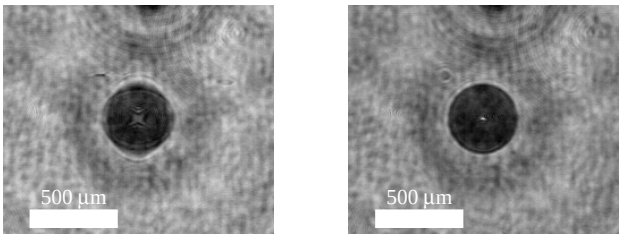

(a) (b)

Figure 5. Numerically refocused amplitude image (z = 211.96 mm) within the solid white box in Figure 4(b), (a) using the normal Rayleigh-Sommerfeld diffraction kernel, Eq. (6), and (b) an aberration compensated kernel, Eq. (7).

In the hologram recording process, the light wave passes through oil-glass and glass-air refraction interfaces, whereas in the reconstruction process the numerical propagation is conducted in a uniform medium (air). This introduces a systematic error in locating the particle, which can be studied by analyzing the image of a point light source reconstructed from an in-line hologram. The modeled system is illustrated in Figure 6. A point light source located at (x_0', y_0') gives rise to an object wave, which is found from the Collins formula under paraxial approximation,[14]

$$E_o(\xi,\eta)=\frac{\exp(jkz_{axis})}{j\lambda C}\int_{-\infty}^{+\infty}\int_{-\infty}^{+\infty}\delta(x'-x_0',y'-y_0')\exp\left\{\frac{jk}{2C}\left[(x'-\xi)^2+(y'-\eta)^2\right]\right\}dx'dy', \tag{8}$$

where $C = z_1/n_1+z_2/n_2+z_3/n_3$ is derived from the ray matrix of the system enclosed by the red dotted rectangle in Figure 6; and $z_{axis} = n_1z_1+n_2z_2+n_3z_3$ is the optical path along the optical axis. Given the property of the delta function, Eq. (8) can be written as

$$E_o(\xi,\eta)=\frac{\exp(jkz_{axis})}{j\lambda C}\exp\left\{\frac{jk}{2C}\left[(x_0'-\xi)^2+(y_0'-\eta)^2\right]\right\}. \tag{9}$$

In the reconstruction process, the fourth term in Eq. (2) produces a real image of the point light source. Propagation of that term via Eq (4) gives

$$E'(x,y,z)=P\int_{-\infty}^{+\infty}\int_{-\infty}^{+\infty}\exp\left\{-\frac{jk}{2C}\left[\xi^2+\eta^2-2(x_0'\xi+y_0'\eta)\right]\right\}\exp\left\{\frac{jkn_3}{2z}\left[(\xi-x)^2+(\eta-y)^2\right]\right\}d\xi d\eta, \tag{10}$$

where E' denotes the complex amplitude propagated from the fourth term only, and $P = n_3|E_r|^2\exp\{jk(n_3z-z_{axis}-(x_0'^2+y_0'^2)/2C)\}/(\lambda^2Cz)$. From Eq. (10), the real image of the point light source is in focus when $z = n_3C$, and E' is reduced to a delta function, expressed as

$$E'(z=n_3C)=|E_r|^2\exp\left\{jk\left(\frac{n_3^2-n_1^2}{n_1}z_1+\frac{n_3^2-n_2^2}{n_2}z_2\right)\right\}\delta(x-x_0',y-y_0'). \tag{11}$$

Note, the lateral coordinates in the image (x_0', y_0') are identical to those of the point light source, while the in-focus z-position of the particle (distance from the hologram plane to the image plane) is related to the actual distances by

$$z = n_3C = n_3z_1/n_1 + n_3z_2/n_2 + z_3. \tag{12}$$

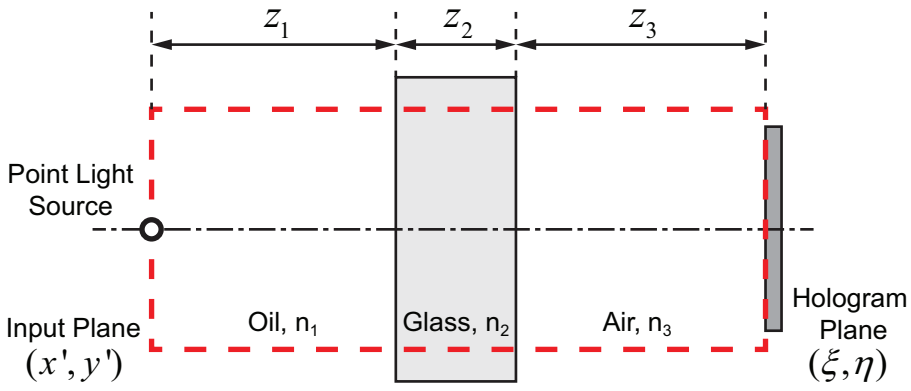

Figure 6. Illustration of the simulated digital in-line hologram of a point light source used to investigate the systematic error of z-location measurement due to refraction interfaces.

Here, we further assume that the thickness of the glass, z_2, is small and its effects can be ignored. Further, the index of refraction of air, n_3 =1. With that, the corrected distance, z_c, from the hologram to the particle becomes,

$$z_c = z_1 + z_3 = n_1\left(z - z_3\right) + z_3, \tag{13}$$

where n_1 = 1.403 and is the index of refraction of the silicone oil. $z_3 \approx 190$ mm and is the distance from the hologram to the first surface of the cuvette. In the results that follow, all of the reconstructed z-positions have been corrected using Eq. (13).

IV. Experimental Results and Discussion

The literature contains a number of methods which search throughout the reconstructed z-location and automatically measure in-focus features.[5-8] Here, we focus on one such method in order to illustrate the results which can be obtained from the proposed experimental configuration. In Guildenbecher *et al.*[7] we outline a *hybrid method* of particle detection. In this method, in-focus features are located by searching throughout depth using Eq. (5). Features which show a simultaneous minimum of intensity within their interior and a maximum sharpness gradient along their outside edge are automatically extracted. Full details on the method implementation can be found in Guildenbecher *et al.*[7] and Gao *et al.*[8] The hybrid method has been applied to quantify the breakup of a drop in an aerodynamic flow[9] and the impact of a drop on a thin film.[3]

Here, the hybrid method is applied by reconstructing 2001 planes evenly spaced between $z = 150$ mm to $z = 250$ mm. For the case where $\bar{d} = 465$ μm, valid features are extracted with an area equivalent diameter, d, $300 \le d \le 1000$ μm. Likewise for the case where $\bar{d} = 118$ μm, valid features are extracted with $50 \le d \le 400$ μm. These ranges are chosen to span the expected range of particle diameters while minimizing detection of false regions due to noise. Further, to eliminate particles which overlap in the x-y plane and are incorrectly detected as single large particles, no region is accepted with an eccentricity greater than 0.5. Finally, as described in Gao *et al.*[8] the hybrid method is first applied using the minimum amplitude map and then refined using the local amplitude detected in the first iteration.

Figure 7 shows the detected particle images from the holograms shown in Figure 4. Here, the shapes represent the particle morphologies measured in the x-y plane while the color gives the measured z-position, corrected for index of refraction using Eq. (13). From all hologram images, the measured mass median diameter is 457 μm and 128 μm for the cases where $\bar{d} = 465$ μm and $\bar{d} = 118$ μm, respectively. This represents an error of -1.7% and 8%, respectively. Furthermore, the mean measured particle concentration is 3.0 particles/cm^3 and 2.3 particles/cm^3, for the cases where $\bar{d} = 465$ μm and $\bar{d} = 118$ μm, respectively. Recalling that the actual particle concentration is around 3.3 particles/cm^3 and 2.9 particles/cm^3 for the $\bar{d} = 465$ μm and $\bar{d} = 118$ μm cases, respectively, these results give some indication of the percentage of the particles which have been invalidated due to overlap.

Figure 7 also shows the measured x-y trajectory of the particle highlighted by the white boxes in Figure 3. Notice, as time progress from left to right, the particle first moves in the positive x-direction, reaches a maximum, and then traverses back in the negative x-direction. This is indicative of the expected circular motion about the stir rod. Assuming that the measured x-positions display minimal error, the x versus t results can be fit to the following expression in order to find the radius, r, and angular velocity, ω, of the selected particle.

$$x(t) = r\cos\left(\omega t + \theta_0\right). \tag{14}$$

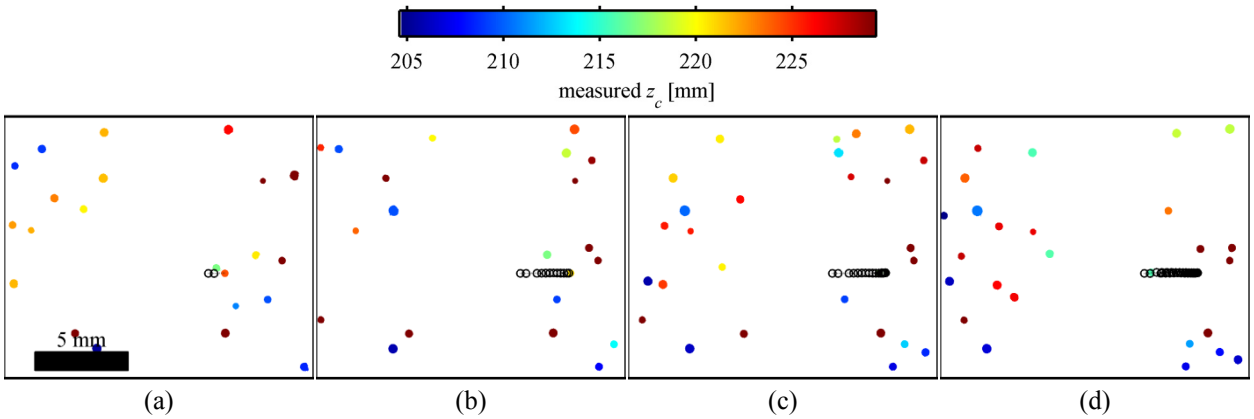

Figure 7. Reconstructed particle images corresponding to the holograms shown in Figure 4. Circles connected by lines show the detected trajectory of the highlighted particle from all previous realizations.

Here, θ_0 is the initial angular position of the particle. Non-linear regression is used to find r, ω, and θ_0 from the measured x versus t. For the trajectory highlighted in Figure 7, this results in $r = 5.04$ mm and $\omega = 9.414$ rpm, with a goodness of fit quantified by $R^2 = 0.9996$. Further, from the simulations in Figure 3, the angular velocity at this value of r is predicted to be 9.406 rpm. Good agreement between the curve fit value and the prediction indicates that the proposed method of fitting the measured x versus t trajectory to the predicted behavior results in an accurate measure of r and ω for a given particle.

This process is repeated for all measured particle trajectories, accepting any curve-fit with an R^2 value greater than 0.99. For the case where $\bar{d} = 465$ mm, 36 particle trajectories are validated in this manner, and Figure 8 shows the measured r versus ω compared with the prediction. Again, good agreement between measured and predicted values is observed. Finally, the process is repeated for the case where $\bar{d} = 118$ μm, where 21 valid particle trajectories are found (not shown).

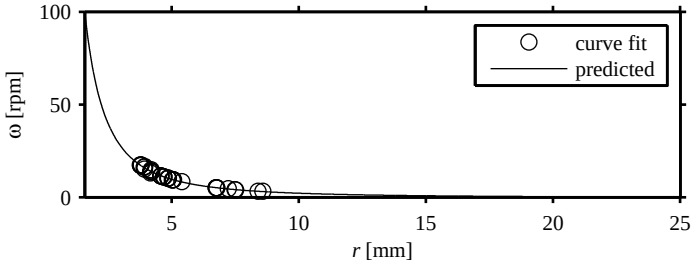

Figure 8. Angular velocity versus radius from the curve fit of measured x versus t trajectories using Eq. (14) for the case where $\bar{d} = 465$ mm compared with the predicted values from simulation.

With the estimates of r and ω for a given particle, a theoretical relationship for the z-position can now be obtained as

$$z(t) = r\sin(\omega t + \theta_0). \tag{15}$$

For example, Figure 9 compares the measured x-z positions of the particle highlighted in Figure 7 with the predicted values from the curve fit (Eqs. (14) and (15)). Notice, in addition to the trajectory measured to the right of the rod (as highlighted in Figure 7) Figure 9 shows a second trajectory of this same particle which has been measured at a later time when the particle is visible to the left of the rod.

Figure 9 illustrates the advantages of the proposed experimental configuration. From experimental DIH measurements alone, it is possible to validate both the measured z-position as well as the measured Δz, where the theoretical Δz is given by

$$\Delta z(t) = r\omega\cos(\omega t + \theta_0)\cdot\Delta t\,. \tag{16}$$

Here Δt is the time between DIH measurements. For the trajectories shown in Figure 9 the mean error in z (measured - theoretical) is -0.0683 mm with a standard deviation of 0.3128 mm. Likewise, the mean error in Δz (measured – theoretical) is 0.0260 mm with a standard deviation of 0.2068 mm.

Furthermore, comparison between the measured and predicted trajectories in Figure 9, gives some indication of the major sources of uncertainty which affect the positioning accuracy. For example, the larger deviation of the measured trajectory in the upper right in Figure 9 ($x = 3$ mm, $z = 224$ mm), corresponds to a time when the measured particle is in close proximity to other particles in the x-y plane (see Figure 7(a) and Figure 4(a)). This indicates that particle z-positions as measured by the hybrid method are susceptible to larger uncertainty when neighboring particles interfere with the diffraction field of the measured particle. While this conclusion is somewhat expected, in the future it may be possible to use the results to define alternative methods which are less susceptible to this error source.

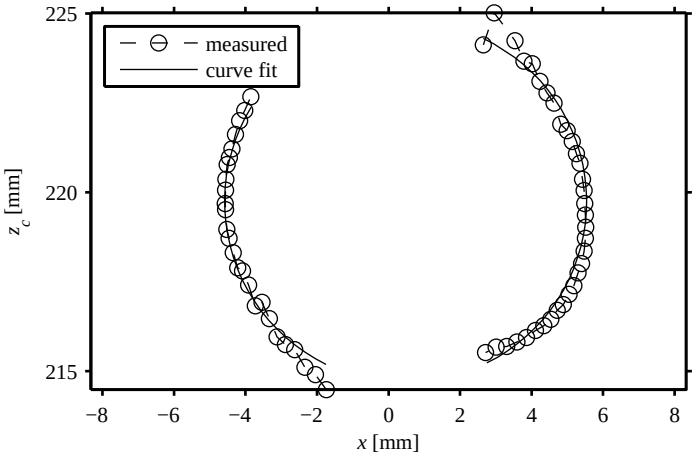

Figure 9. Measured x-z trajectory of the particle highlighted in Figure 7 along with predicted trajectory from the curve fit.

Finally, Table 1 summarizes the mean and standard deviation in the error in the measured z-positions and displacements for the two cases considered here. For all quantities, the mean error is small, signifying little bias in the measured quantities. This indicates that it should be possible to calculate accurate flow averages from multiple DIH realizations and the hybrid method. On the other hand, the z-uncertainty, as quantified by the standard deviation, is relatively high, as expected due to the aforementioned depth of focus problem.[2] For this reason, higher order flow statistics as measured by DIH should be calculated and interpreted with great care. Finally, the uncertainty in measured Δz is on the order of 2.3-2.6 mean particle diameters. Our previous measurements using stationary particle fields with uniform displacements resulted in an estimated uncertainty on the order of 1.5-1.7 mean particle diameters. This indicates that the experiments performed here, which include relative motion between particles, incorporate additional sources of experimental uncertainty.

Table 1. Mean ± standard deviation of the error in measured particle z positions and displacements.

	$\overline{d}$ = 118 μm	$\overline{d}$ = 465 μm
positional error [mm]	-0.0025 ± 0.3787	0.0405 ± 1.5050
displacement error [mm]	-0.0009 ± 0.3024	-0.0318 ± 1.0481

V. Conclusion

An experimental investigation of the depth (z-position) uncertainty in digital in-line holography (DIH) is presented. Experimental methods are proposed wherein a slowly rotating particle field with well-defined particle trajectories is used to derive the theoretical z-position of individual particles. This allows for quantification of z-uncertainty directly from the measured results. Specific conclusions from the results reported here include:

- Proposed corrections for the effects of refractive interfaces along the beam path result in measured z-positions with mean behavior matching the predicted trajectory.
- For this flow configuration, a curve fit to the in-plane (x-y) displacements provides accurate estimates of the circular trajectories of individual particles. From this, a predicted value of out-of-plane z-position can be derived and compared to measurements.
- Measurement of these flow conditions with DIH and the hybrid method of particle detection indicates accurate quantification of the mean z-positions and uncertainty on the order of 2.5 mean particle diameters.

In the future, this work could be extended to compare the experimental accuracy of various particle detection methods. This would allow one to quantify those aspects of each method that are most susceptible to uncertainty and possibly derive new methods with reduced uncertainty. Finally, additional work should be undertaken to repeat these experiments with minimized aberrations, such that the *ad-hoc* corrections for the observed astigmatism can be eliminated.

Acknowledgments

Sandia National Laboratories is a multiprogram laboratory operated by Sandia Corporation, a Lockheed Martin Company, for the United States Department of Energy's National Nuclear Security Administration under contract No. DE-AC04-94AL85000.

References

1. Schnars, U., and Jueptner, W. *Digital holography: Digital hologram recording, numerical reconstruction, and related techniques*. Berlin: Springer, 2005.
2. Katz, J., and Sheng, J. "Applications of holography in fluid mechanics and particle dynamics," *Annual Review of Fluid Mechanics* Vol. 42, 2010, pp. 531-555.
3. Guildenbecher, D. R., Engvall, L., Gao, J., Grasser, T. W., Reu, P. L., and Chen, J. "Digital in-line holography to quantify secondary droplets from the impact of a single drop on a thin film," *Experiments in Fluids* Vol. Accepted for publication, 2013.
4. Meng, H., Pan, G., Pu, Y., and Woodward, S. H. "Holographic particle image velocimetry: from film to digital recording," *Measurement Science and Technology* Vol. 15, No. 4, 2004, p. 673.
5. Tian, L., Loomis, N., Domínguez-Caballero, J. A., and Barbastathis, G. "Quantitative measurement of size and three-dimensional position of fast-moving bubbles in air-water mixture flows using digital holography," *Appl. Opt.* Vol. 49, No. 9, 2010, pp. 1549-1554.
6. Yang, Y., Li, G., Tang, L., and Huang, L. "Integrated gray-level gradient method applied for the extraction of three-dimensional velocity fields of sprays in in-line digital holography," *Applied Optics* Vol. 51, No. 2, 2012, pp. 255-267.

7. Guildenbecher, D. R., Gao, J., Reu, P. L., and Chen, J. "Digital holography simulations and experiments to quantify the accuracy of 3D particle location and 2D sizing using a proposed hybrid method," *Applied Optics* Vol. 52, No. 16, 2013, pp. 3790-3801.
8. Gao, J., Guildenbecher, D. R., Reu, P. L., and Chen, J. "Uncertainty characterization of particle depth measurement using digital in-line holography and the hybrid method," *Optics Express* Vol. 21, No. 22, 2013, pp. 26432-26449.
9. Gao, J., Guildenbecher, D. R., Reu, P. L., Kulkarni, V., Sojka, P. E., and Chen, J. "Quantitative, 3D diagnostics of multiphase drop fragmentation via digital in-line holography," *Optics Letters* Vol. 38, No. 11, 2013, pp. 1893-1895.
10. Notz, P. K., Subia, S. R., Hopkins, M. M., and Noble, D. R. "ARIA Manual Aria 1.5; User's Manual." Sandia National Laboratories, Albuquerque, NM, 2007.
11. Moffat, H. K. "Viscous and resistive eddies near a sharp corner," *Journal of Fluid Mechanics* Vol. 18, 1964, pp. 1-18.
12. Pan, F., and Acrivos, A. "Steady flows in rectangular cavities," *Journal of Fluid Mechanics* Vol. 28, No. 4, 1967, pp. 643-655.
13. Nicola, S. D., Ferraro, P., Finizio, A., and Pierattini, G. "Wave front reconstruction of Fresnel off-axis holograms with compensation of aberrations by means of phase-shifting digital holography," *Optics and Lasers in Engineering* Vol. 37, No. 4, 2002, pp. 331-340.
14. Collins, J. S. A. "Lens-system diffraction integral written in terms of matrix optics," *Journal of the Optical Society of America* Vol. 60, No. 9, 1970, pp. 1168-1177.